LASER SINTERING PROCESS OF CERAMIC POWDERS: THE EFFECT OF PARTICLE SIZE ON THE MECHANICAL PROPERTIES OF SINTERED LAYERS

Daniele Sofia, Diego Barletta, Massimo Poletto*

Dipartimento di Ingegneria Industriale, Università degli Studi di Salerno, Via Giovanni Paolo II, 132, 84084 Fisciano (SA), Italy

*Corresponding author. Tel. +39 089962499; Fax +39 089964057;E-mail address: mpoletto@unisa.it

Abstract

In this paper we study the Selective Laser Sintering (SLS) process of ceramic powders. The aim is to understand how the initial material properties and the process conditions affect the degree of sintering/melting and the mechanical properties of the sintered material. Unimodal powder samples of different narrow particle size distributions between 16 and 184 μm were sintered with a 40W CO_2 laser, using laser scan speeds of either 5 or 10 mm s^{-1}. The sintered material was studied by means of microphotography and characterized in terms of bulk density and tensile strength. The Rumpf approach modified according to Molerus was used to estimate the average strength of the sintered interparticle contacts starting from the tensile strength of specimens. In turn, the average strength of the neck contact was used to estimate the size of the neck of fused material between to sintered particles. These data coupled with the Frenkel model allowed an estimate of the sintering temperature for the different experimental conditions tested. The temperatures found are consistent with the glass transition temperature of the material used. The effect of particle size and scanning speed is assessed and discussed.

Keywords: Laser sintering; ceramic powders; particle size; mechanical properties; Frenkel model.

* Corresponding author. Tel. +39 089962499; Fax +39 089964057

E-mail address: mpoletto@unisa.it

1. Introduction

In recent years, additive manufacturing technologies are changing production processes in many sectors such as: biomedical [1–3], metallurgical [4–6], aerospace etc. Some of the most promising processes are Selective Laser Sintering (SLS) and Selective Laser Melting (SLM), in which a controlled laser beam is used for sintering/melting of powders. In particular, three dimensional objects can be obtained by means of a layer by layer additive technique. Consequently, significant advantages of these additive manufacturing technologies with respect to traditional sintering processes [7–9] are given by the possibility of advanced product customization and of complex internal morphology of the artefacts [10]. The discrimination between SLS and SLM is labile and it is mostly related to the amount of energy released to the material by the laser beam during the sintering/melting process [11]. An advantage of SLS versus SLM lies in smaller contraction of the processed material due to the limited change in the particulate solids. Therefore, SLS is a more promising technique for the production of high accuracy sized objects. Furthermore, SLS allows the production of artefacts with internal porosity, a valuable property that is required in some applications, such as the production of scaffolds for medical use [12]. It is of interest, therefore, the understanding of how the initial material properties and the process conditions interact with each other to determine the degree of sintering/melting of the raw material powder, as well as the sintered material mechanical properties. Most of the relevant investigations in the literature show that laser sintering is a very complicated process [13], with several parameters influencing the densification mechanism and affecting the final microstructural features.

Most of the current applications of SLS and SLM make use of metal [14,15] or polymeric powders [16–19]. Most recent developments of these technologies have allowed to create functional objects directly from metal powders without using either post-processing operations or binders (low melting additives) [20]. A significant further spread of the application of these technologies can derive from the use of ceramic materials [21]. The main issue with ceramic materials processing is the quality

50 improvement of the manufactured products [22]. In particular, size accuracy, strength and surface
51 finish of sintered parts are significantly affected by the type of material and by the process parameters
52 [23,24]. In fact, laser sintered artefacts are generally fragile and characterized by low density and
53 poor surface finish. Fragility of SLS/SLM artefacts is mainly due to high residual stresses in the
54 internal structure of the objects, resulting from the high temperature spatial non-homogeneity
55 determined by the process. In general, in all sintering processes the fragility of the artefact depends
56 on the strength of the interparticle solid necks resulting after solidification of molten contact zones
57 between particles [25]. This strength depends on the process parameters and mainly on the operating
58 temperature and pressure during the sintering process. For example, Luan et al. [26] found that the
59 neck tensile strength of sintered ash particles increases with the bonding time and pressure. Additional
60 influencing process parameters of SLS and SLM are given by the laser power and scan rate, the
61 scanning line spacing, the thickness of powder layers, the scanning geometry, the working
62 atmosphere, the powder bed temperature. Moreover, powder properties like particle material, particle
63 size distribution and particle shape play an important role on the final artifact characteristics as well
64 [27, 28].The mechanical strength characterization of the artefacts includes the use of compression
65 [23] or bending [21] tests. In particular this latter can be applied to single layer objects, while the
66 former requires well defined 3D structures. In any case, destructive tests can used to understand the
67 mechanical properties of the sintered artefacts [29]
68 Another important issue of the SLS process is the object shrinkage. This is influenced by material
69 and process parameters as well as by the geometry of the manufactured object. The object size and
70 shape inaccuracy due to shrinkage is generally overcome by calibrating the process and compensating
71 for it in the design of the initial powder bed specimen. Further improvements in the accuracy of the
72 manufactured object can be achieved by appropriate studies carried out to appreciate the sources of
73 the object size deviations, in order to adjust the calibration procedure to the process conditions [30].
74

The aim of the present work is to study the effects of some process parameters and powder properties on the dimensions, the weight and the mechanical properties of the final sintered artefacts. In particular,. the study is focused on the effect of the laser power and the average particle size of ceramic powders on the tensile strength the sintered materials. The application of a micromechanical model allows to derive the interparticle neck size from the measured tensile strength.

2. Experimental methods

2.1 Apparatus

The apparatus used in this work is reported in Figure 1a. It mainly consists of a laser tube and a system to collimate the laser beam in order to hit in a precise position of the powder surface. In particular, the CO_2 laser tube emits beams at a wavelength of 10.6 μm with a spot size of 100 micron diameter and a maximum power of 40 W. The collimating device is made of a couple of inclined mirrors moving on the x-y plane as shown in the figure. This system allows to change the laser scan velocity in a range between 1 mm s^{-1} and 100 mm s^{-1}. The nominal laser power of 40 W is sufficiently high to allow the melting of ceramic materials in powder form. Adjusting the laser power and its speed it is possible, therefore, to control the process in order to obtain melting or sintering of the powder material. In principle, three dimensional objects might be obtained with the addition of new material to be sintered in subsequent layers. The procedure generally used in commercial processes includes the lowering of the powder sample, the spread and possibly the consolidation of the new material on top of it, to re-establish the original powder height at the laser focal plane. The amount of lowering defines the thickness of the fresh powder layer, that has to be thin enough to be effectively sintered by the laser beam in its whole thickness. However, only the results obtained by working on a single layer of sintered powder will be reported in this paper.

A special apparatus was used to consolidate and level beds of powders before sintering. The apparatus is shown in Figure 1b and it consists of a flat lid connected by means of a cylindrical rod to a loading

plate. The vertical rod can freely move in linear bearings which allow the rod to move vertically and to rotate around its axis. The rod has a loading plate on the upper end. This apparatus allows the application of a pre-defined stress to the material below the lid, by applying the correct load on the upper plate, and contemporarily, the use of a twisting action, obtained by rotating the rod with the help of a lever.

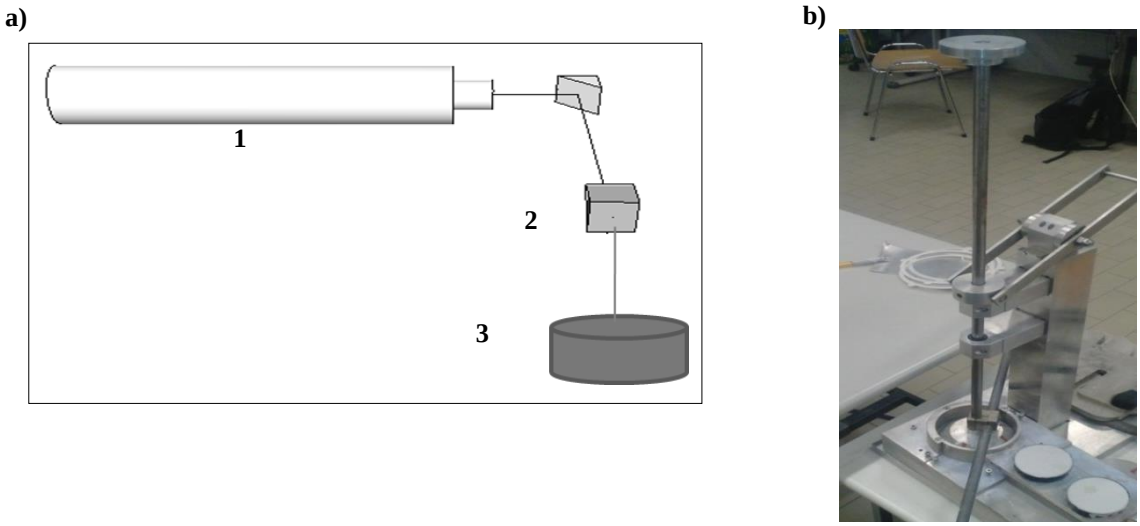

Figure 1. Experimental set-up. a) Apparatus for laser sintering: 1. laser tube; 2. scanning mirrors moving in x and y directions; 3. laser beam; b). Apparatus to consolidate and level beds of powders before the sintering process.

2.2 Preparation of powder specimens

Glass beads, made of a soda-limestone glass, taken from three batches each characterized by a wide particle size distribution (PSD) (<50 μm; 10 to 100 μm; 100 to 200 μm) were sieved in order to obtain samples characterized by narrow PSD. For each of the sieved samples, Table 1 reports the nominal ranges of the particle size of the original batches, the undersize and oversize sieve meshes used to produce each sample, the mean Sauter diameter, d_s, of the sample measured by means of a laser scattering measurement device (Malvern Mastersizer 2000), as well as the bulk density of the sample. The particle density was measured with a helium pycnometer and it is equal to 2500 kg m^{-3}.

Table 1. Properties of sieved samples of glass beads.

Original cut size range, µm	Sieving range, µm	$d_s[3,2]$ μm	$d[4,3]$ μm	d_{10} μm	d_{50} μm	d_{90} μm	ρ_b kg m^{-3}
<50	< 25	16	15	10	15	20	1368
<50	25-32	27	28	17	25	34	1404
10-100	32-63	45	49	31	47	63	1504
100-200	63-125	86	87	56	85	114	1524
100-200	125-180	160	162	102	157	207	1536
100-200	160-250	184	182	119	180	241	1540

2.3 Sintering procedure

Single layer squared specimens (10x10 mm) of sintered materials were obtained in the laser apparatus described above. Prior to each sintering test, cylindrical beds of powder samples were levelled and consolidated at 2.5 kPa and two 90° twists operated by means of the powder consolidation apparatus described above. The sintering of squared specimens was obtained by moving the laser on fifty one 10 mm long parallel lines at a distance of 0.2 mm from each other.

The laser scanning speed and the laser power were set according to two alternative combinations of values to provide the same scanning energy of 160 J m^{-1}. In particular, the first settings are given by a laser beam power of 8 W and a scan speed of 50 mm s^{-1}, while the second ones are given by a laser beam power of 16 W and a scan speed of 100 mm s^{-1}..

After the sintering process sintered specimens were gently extracted from the powder bed. Particles loosely adhering to the sintered specimen due to van der Waals forces were softly removed by means of a paint brush. The weight of sintered specimens was measured with an analytical balance (300 Crystal).

2.4 Bending tests

Bending tests were carried out on the square shaped sintered specimens to relate the sintering process parameters to the tensile strength of the obtained artifacts. The tests consist in following the three point bending flexural method as sketched in Figure 2a. The instrument used to measure forces and

displacements is an Instron 5865 dynamometer equipped with a load cell of 2.5 N. Given the small size of the samples, a specifically designed tool, represented in Figure 2b, had to be used. The upper horizontal edges of two vertical plates kept at a known distance by two screws act as lower supports for the bending test. The blade hold at the tip of the load cell stem act as the upper bending tool.

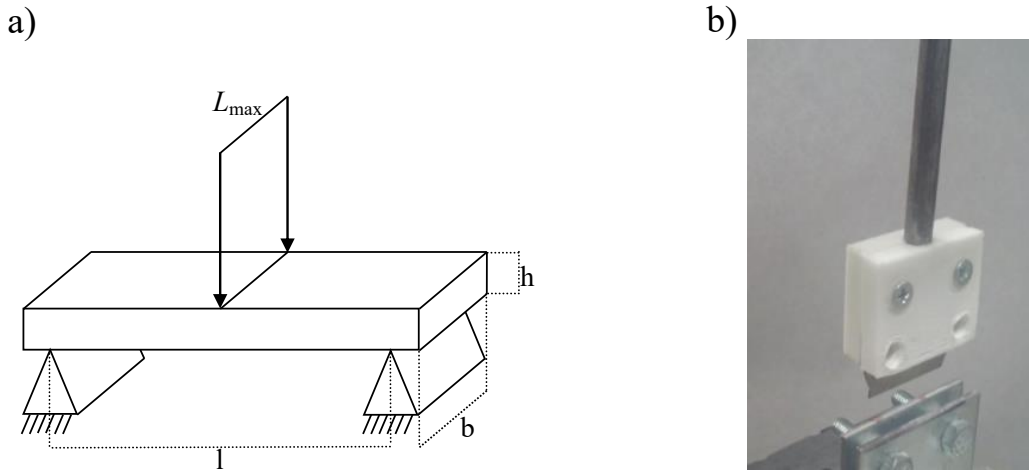

Figure 2. Three point bending test: a) Schematic; b) Bending tool.

A typical example of force displacement curve is reported in Figure 3. The x-axis reports the height of the edge of the upper bending tool above the holder, the y-axis reports the force measured by the upper bending tool. The layer thickness, *t*, can be derived from the difference between the height at which the bending tool starts to detect a finite force and the height of the supports. The peak force, L_{max}, identifies the sample breakage. Assuming a rectangular geometry of the sintered specimen the following equation can be used to relate the breakage force to the tensile strength, $\sigma_{b,}$ of the sintered material:

$$\sigma_b = \frac{M_b}{I}\frac{h}{2} = L_{max}\frac{3l}{2bt^2} \quad (1)$$

where M_b is the bending moment, I is the horizontal moment of inertia of the sample vertical cross section, h is the layer deflection, b is the specimen width, l is the distance between the supports.

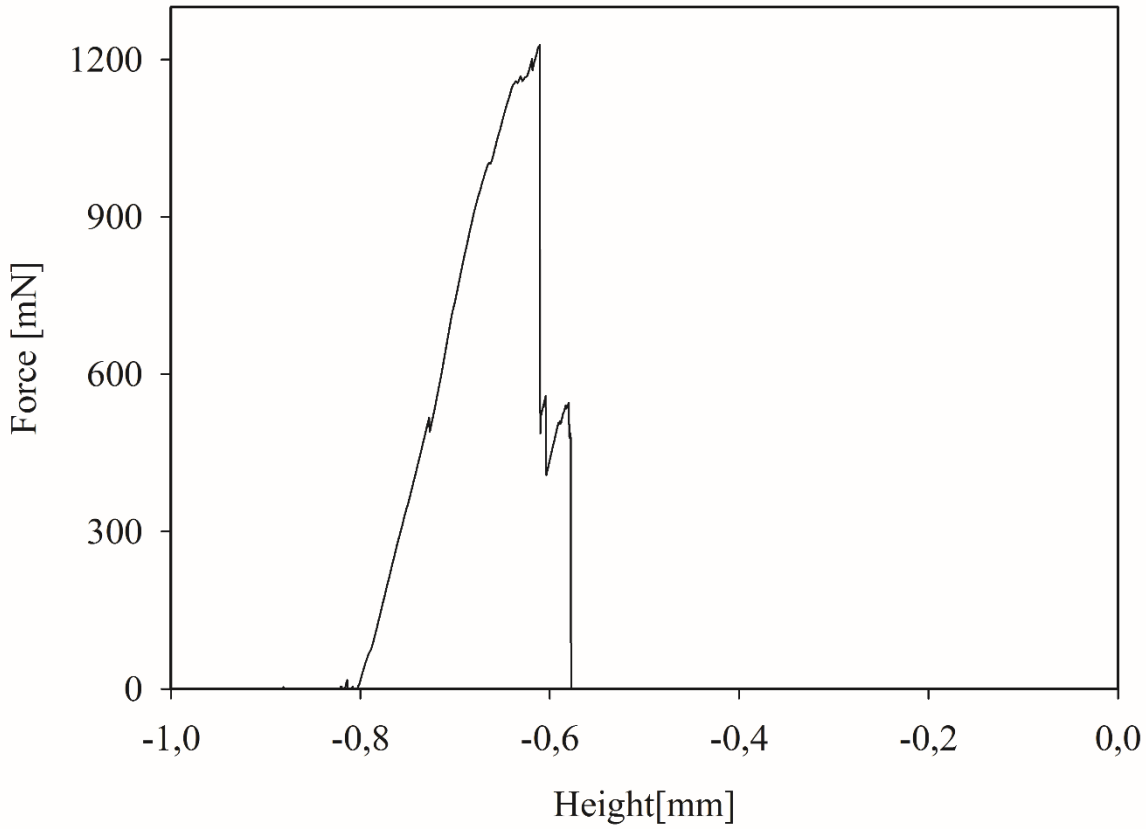

Figure 3. An example of a force vs displacement curve in a bending test.

3. Experimental results

3.1 Unimodal layers

Figure 4 reports macro and micro photographs of the sintered specimens using a laser beam of 8 W and a scan speed of 50 mm s^{-1}. In the Figure, organized in the form of a table, each row corresponds to a different mean diameter of the initial powder sample. The table starts with the finest sample (d_s=16 µm) indicated with letter a) and ends with the coarsest sample (d_s=184 µm) indicated with letter f)., Macro photographs of the whole 10x10 mm specimens are reported in column M of the Figure, while columns F, R and T report optical microscopy pictures (about 100x) of the sintered specimens, respectively the front (the laser sintering side) view, the back view and the lateral view.

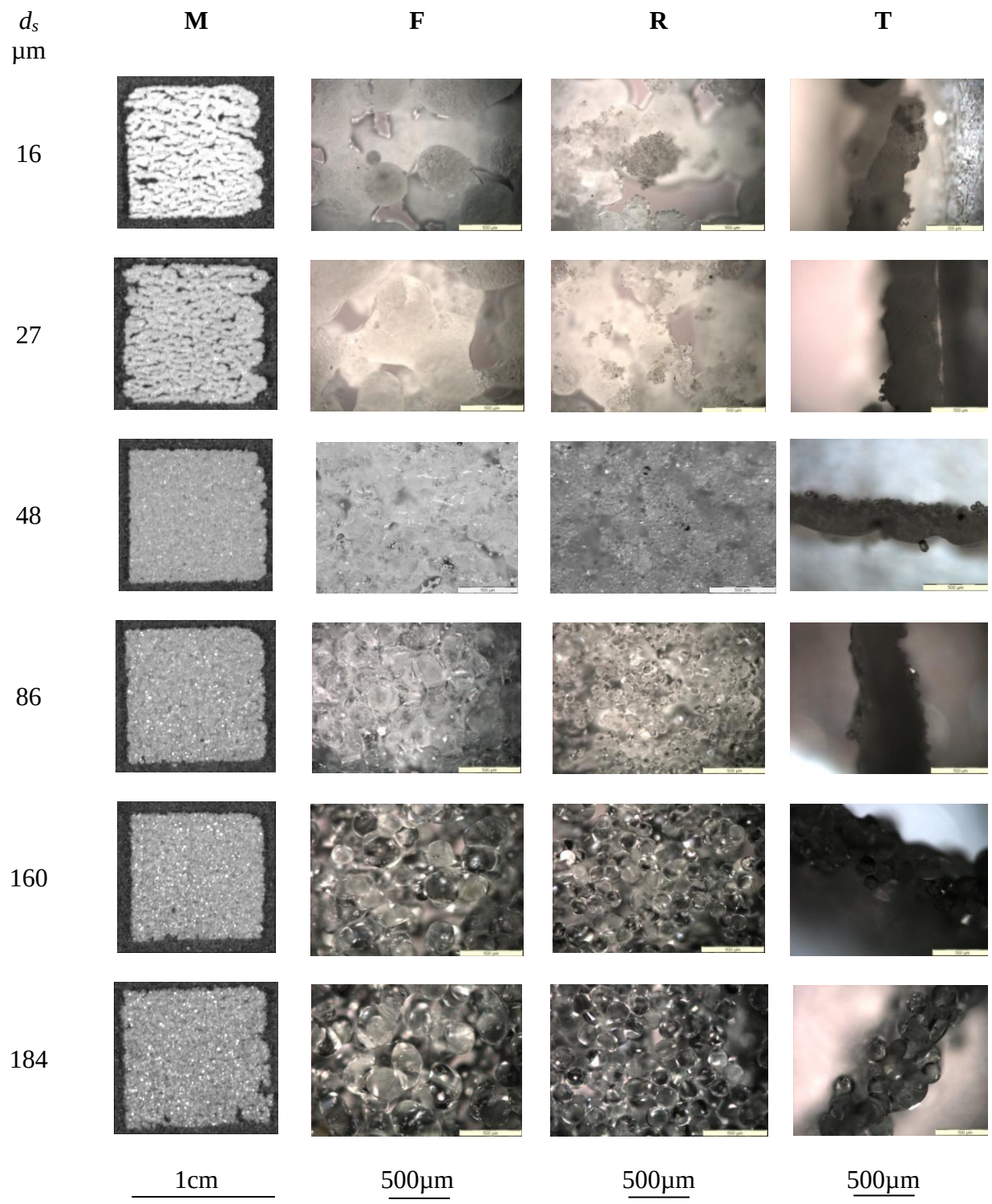

Figure 4. Macro and micro photographs of 10x10 mm sintered specimens obtained from narrow PSD powder samples of different mean particle size *d*, by using a 8 W laser beam and a 50 mm s^{-1} laser scanning speed. M macroscopic view; F, front view; R back view; T, lateral view.

Inspection of Figure 4 indicates that the particle size of the powder sample significantly affects the final morphology of the specimen by means of the extent of the molten zone with respect to the initial

particle dimensions. In particular, inspection of the front views (F) indicates that for finer powders (d_s=16 μm and d_s=27 μm) whole particles melted and, thus, the initial particle size and shape vanished in the final solidified specimen made out of lumps. Instead, for coarser powders (d_s=160 μm and d_s=184 μm) melting was limited to interparticle contact zones and, thus, a final sintered specimen with unchanged primary particle size and shape was obtained. Intermediate morphology was obtained for powders with d_s=48 μm and d_s=86 μm. Moreover, inspection of the microscopic back view (R) of the specimens reveals the existence of regions of non-fused primary particles adhering to the fused material. This evidence would suggest a non uniform laser energy transfer through the specimen thickness. In particular, pictures of the specimens obtained from powder samples of 48 μm and 86 μm seem to show melting on the front side and sintering on the back side. In the latter case a continuous layer of sintered particles can be observed. Pictures of the specimens from powder samples of 160 μm and 184 μm suggest that sintering is the predominating mechanism on the whole layer thickness and that only some traces of melting are still visible on the front layer in form of particles somewhat larger than the primary. This phenomenon might be reasonably attributed to the coalescence of smaller fused particles during the process.

These results clearly indicate an effect of the particle size on the melting ability of the laser beam. However, lateral views of the specimen (T) do not show significant differences in the thickness of the specimen, suggesting that the penetration depth of the laser beam is comparable for all the tested powders with different particle size. Further evidences on the effectiveness of laser penetration are provided with the results of specimen weight, and of layer thickness, reported in Figure 5a and 5b respectively. Inspection of Figure 5a reveals that the specimen weight tends to increase with increasing particle size up to d_s=160 μm, where melting is the prevailing phenomenon, and keeps almost constant for larger particle sizes (d_s=160 μm and d_s=184 μm), where sintering is occurring. Layer thickness was measured in bending tests, according to the procedure explained in section 2.4. Results reported in Figure 5b confirm that the specimen thickness does not change significantly with the particle size in the range 27-160 μm. The smallest value of thickness was recorded for d_s=16

198 μm, while the largest value was measured for d_s=184 μm. Further inspection reveals that error bars
199 for specimens produced with finer powders (d_s=16-48 μm) are of the order of magnitude of the
200 particle size. This result might be explained with the adhesion of few particles on the specimen surface
201 due to van der Waals forces. In fact, van der Waal forces for rounded particles are comparable to the
202 particle weight up to diameters of the order of 100 μm (i.e page 124 [25] in Seville et al 1997).
203 As above mentioned, commenting results reported in Figure 4, the sintering process presents uneven
204 results along the thickness of the sintered specimen. In the bending test the specimen was positioned
205 on the supports keeping the orientation defined by the sintering process. This allowed measuring the
206 tensile strength of the material on its weaker side, that is the downward side. Tensile strength data
207 measured with this procedure are reported in Figure 5c. Inspection of the Figure reveals that the
208 tensile strength of the material presents a local maximum at 48 μm. The tensile strength decreases
209 considerably for larger particle diameters with an almost tenfold reduction for the specimen sintered
210 from 184 μm particles with respect to specimen sintered from 27 μm particles. This reduction may
211 be attributed to two different causes: 1) the reduction of the number of sintered interparticle contact
212 points per unit volume with increasing particle size and 2) the reduced strength of single sintered
213 interparticle contacts due to different effects of the sintering process on particles of different sizes.
214 For simplicity, in the following the sintered contacts will be referred to as “necks”. Furthermore, as
215 discussed above, in the results, the obtained sintering of the finest samples, having mean particle
216 diameters between 16 and 27 μm, probably correspond to process condition producing an almost
217 complete melting of the whole specimen thickness. Therefore, this can explain the change of trend
218 for the data relative to these points. In fact, the lower strength for finest particles might be attributed
219 to the lower bulk density of the initial powder, which brings to a looser final structure of the melted
220 material. Similar findings are reported by Tolochko [31] on experiments with SLM.
221 All the above considerations on the optical inspection of sintered specimens and on the measured
222 properties, seem to indicate that the sample characterized by an initial particle size of 48 μm marks a
223 transition between melting and sintering processes, given the laser power and the scanning speed used

in these experiments. All the results seem also to indicate that for specimen produced from powder samples made of 86 µm particles and larger, particle sintering is the prevailing phenomenon.

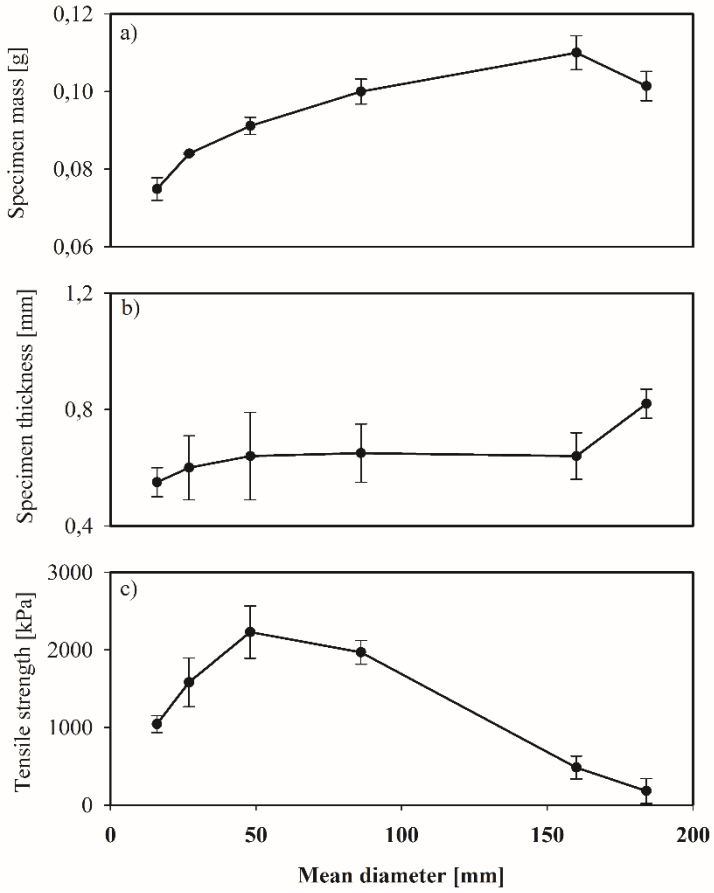

Figure 5. Specimen properties as a function of the particle size of the initial unimodal powder sample:: a) thickness; b) mass; c) tensile strength on the back side. 10x10 mm sintered specimens obtained by using a 8 W laser beam and a 50 mm s^{-1} laser scanning speed.

Specimen properties obtained starting from the same unimodal powder samples and using a double laser scanning speed (laser power of 16W and scanning speed of 100 mm s^{-1}) are reported in Figure 6. Both the specimen mass and the specimen thickness for this case show similar values to those obtained at low speed. Values in this case are just a bit higher for thickness. Furthermore, similarly to the low scanning speed case, in general the specimen mass tends to increase with the particle size, while the specimen thickness shows much more limited variations. Regarding the tensile strength, as expected its order of magnitude in the high scanning speed case is the same to the one obtained in the low speed case, however values in high scanning speed case are generally lower and, in particular for

239 the finest particles. These latter, differently from what observed at low scanning speed, show
240 specimen strength rather close to those of the coarsest particles.
241

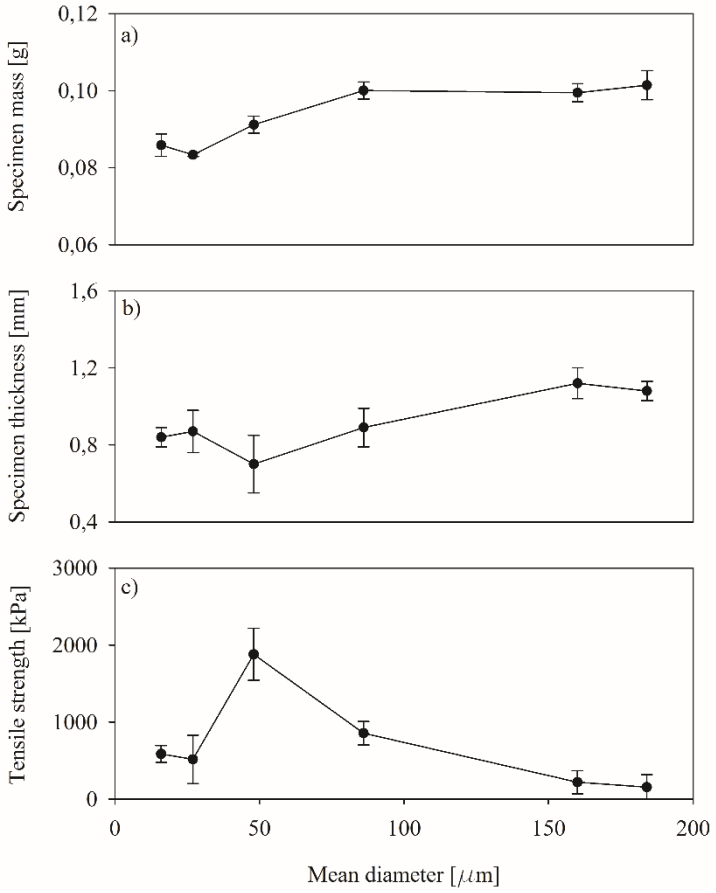

242

243 Figure 6. Specimen properties as a function of the particle size of the initial unimodal powder sample: a)
244 thickness; b) mass; c) tensile strength on the back side. 10x10 mm sintered specimens obtained by using a 16
245 W laser beam and a 100 mm s^{-1} laser scanning speed.
246

247 **4. Discussion**

248 *4.2 Theoretical framework*

249 The macroscopic properties of sintered artifacts will depend upon their microscopic structure, that is
250 the spatial density and the strength of the sintered contacts (necks). It might be argued that, in case of
251 particle sintering, that is in case of limited melting of the particles in the original powder system, the
252 spatial organization of particles can be assumed similar to the initial spatial organization of the

253 particles in the powders prepared for the laser sintering process. For powders a simple approach that
254 allows to relate mechanical properties of powders with the strength of the contact forces between
255 particles is the Rumpf [32] approach modified according to Molerus [33] suggestion, which allows
256 to estimate both the interparticle contact density and their role in the definition of powder strength.
257 The model was originally developed to relate van der Waals forces to powder strength in terms of
258 isostatic tensile stress and it was proven to apply satisfactorily also to uniaxial state of stresses. This
259 model however is sufficiently general to be used to correlate any kind of homogeneous distribution
260 of point contact force, compressive or tensile, on the particle surface to the powder stress,
261 compressive or tensile, locally acting on the powder. Therefore, applying this model at the failure
262 conditions in the following, this approach will be used to relate the tensile strength of the sintered
263 material with the tensile strength of single necks in it.
264 In the Rumpf and Molerus, model some simplifying assumptions are made, in particular it is assumed
265 that:
266 1. particles are organized in a randomly packed assembly and particles are spherical and
267 monodisperse;
268 2. the contact areas between particles are small enough in comparison with the particle surface and,
269 therefore, contact areas can be assumed as contact points;
270 3. the contact points are distributed over the particle spherical surface with equal probability;
271 4. the packing structure is isotropic;
272 5. the transmission of an isostatic state of stress, in which three equal principal stresses are assumed.
273 Starting from these hypotheses, Rumpf [32] and Molerus [33] derived the following equation relating
274 the isostatic stress, σ, with a mean isotropic contact force, F:

275 $$\sigma = F \frac{k_0(1-\varepsilon)}{\pi d^2} \quad (2)$$

276 where d is the particle diameter, ε the particulate system void volume fraction (voidage) and k_0 the
277 particle coordination number. According to the correlation derived by Rumpf [32] from the

experimental data of Smith et al. [34] obtained for spherical particles and values of the particle concentration between 0.55 and 0.65, the empirical relationship $k_0\varepsilon \approx \pi$ is assumed to estimate k:

$$k_0 \approx \frac{\pi}{\varepsilon} \tag{3}$$

Considering the isostatic state of stress as the combination of three orthogonal uniaxial state of stresses Molerus [33] extended the validity of equation (2) also to uniaxial state of stresses.

The simple model reported in equations (2) and (3) will be used to calculate the strength of the necks in the sintered material of the specimen obtained from unimodal powder samples. The detail of this procedure is given in the following.

Considering sintered specimen obtained by sintering materials with unimodal narrow PSD it is possible to use equations (2) and (3) to estimate the strength of the sintered contact F_i for each average particle diameter d_i starting from experimental values of the breakage modulus of the sintered material σ_i

$$F_i = \sigma_i \frac{d_i^2}{(1-\varepsilon_i)} \varepsilon_i \tag{4}$$

the specific void volume fraction ε_i can be related to the experimental powder bulk density, ρ_{bi}, and the particle density, ρ_p:

$$\varepsilon_i = 1 - \frac{\rho_{bi}}{\rho_p} \tag{5}$$

The results of this calculation are provided in Table 2 for both the low and high scanning speed cases. As it is possible to observe from this table, expectedly the particle coordination number k_{0i} is increasing with the system bulk density, but in any case it is much smaller than the theoretical value of 12, proper of the maximum packing density of equally sized spheres. The force of the sintered contact F_i increases with the particle diameter, suggesting larger sintering necks for larger particles and, rather strikingly, it is almost halved in the case of high scanning speed, in spite of the same

scanning energy used in the two tests. Assuming as a reference for the glass tensile strength σ_{tg} a value of 100 MPa it is possible to use the values of F_i to estimate the contact neck size, d_{ci}:

$$d_{ci} = \sqrt{\frac{4F_i}{\sigma_{tg}\pi}} \tag{6}$$

As expected, the contact neck size increases with the particle diameter and, in any case, appears to be fully compatible with the particle diameters. Coherently with the smaller contact forces the neck diameters are smaller in the high scanning speed case.

In the selective laser sintering process the particle coalescence can be described by mechanisms similar to those in conventional sintering. A schematic of two particles in contact, undergoing sintering is shown in Fig.7. One of the earliest models to describe sintering in viscous regime was developed by Frenkel [35], who derived a rather simple expression to describe the time evolution of the neck radius, in which the neck diameter d_{ci} is normalized to the particle size d_i as follows:

$$\left(\frac{d_{ci}}{d_i}\right)^2 = \frac{3}{\pi}\frac{\gamma(T_{gi})}{d_i\eta(T_{gi})}t \tag{7}$$

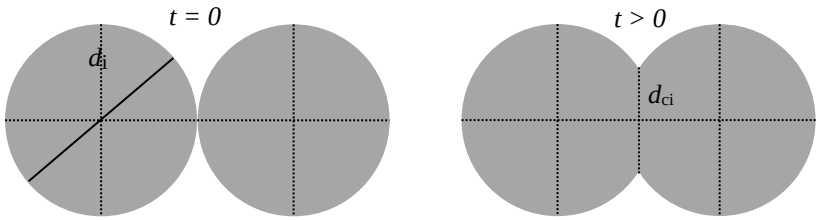

Figure 7 Evolution in time of the dimensionless neck radius.

In the Frenkel model, the sintering rate (or the neck size as a function of time) is dependent on γ, the surface tension, η, the viscosity of the melted material, and t, the sintering time. It states that sintering proceeds faster for materials with a higher surface tension, lower viscosity, and smaller particle radius. However, this model assumes that the particle radius remains nearly constant, and thus it can be valid only for the initial stage of the sintering, when the neck radius is much smaller than the particle radius, i.e. $d_{ci} << d_i$.

Equation (7) puts in evidence the fact that both the surface tension γ and the viscosity μ should be evaluated at the local temperature and, therefore, for its application it is necessary to have the right temperature dependence estimates [36]. Vice versa, equation (7) tells that if we know the neck size, the particle size, the sintering time and the temperature dependence of γ and μ it would be possible to use it to estimate an average temperature in the sintering process. Our glass beads are made of soda lime glass. For this type of materials, the temperature dependence equation is of the kind:

$$\eta = A - \frac{B}{T_g - T_0} \tag{8}$$

according to [37] and assuming a standard composition for the glass (in mass SiO_2 71 % CaO 11%, Na_2O 18%) we adopt A=-2.54 Pa s, B=3810.7 Pa s °C^{-1} and T_0=267.8 °C to calculate η in Pa·s and T in °C. Similarly, with reference to the surface tension, for this kind of glass [38] report values of s, r, t N·m^{-1} at x, y and z °C, respectively. A second order polynomial was used to interpolate these values

$$\gamma = aT_g^2 + bT_g + c \tag{9}$$

with a= 3*10^{-4} N m^{-1} °C^{-2}, b= -0.67 N m^{-1} °C^{-1} and c= 681.83 N m^{-1}. As explained above, Equation (7) to (9) where solved with respect to the temperature given the particle size, the neck size and the sintering time *t.* In the lack of a better estimate this latter was set equal to the particle exposure time to laser t_{exp} that is equal to:

$$t_{\mathrm{exp}} = d_{\mathrm{sp}} / V_{\mathrm{sc}} \tag{10}$$

where d_{sp} is the laser spot size and V_{sc} the laser scanning speed. Figure 8 and Table 2 report the resulting averaged sintering temperatures T_{g} using the neck diameter reported in Table 2. It appears that the estimated sintering temperatures range for all systems between 600 and 700 °C. A maximum of temperature is found for intermediate particle size of the powder used, which is close to the values that provide the maximum strength of the sintered specimen.

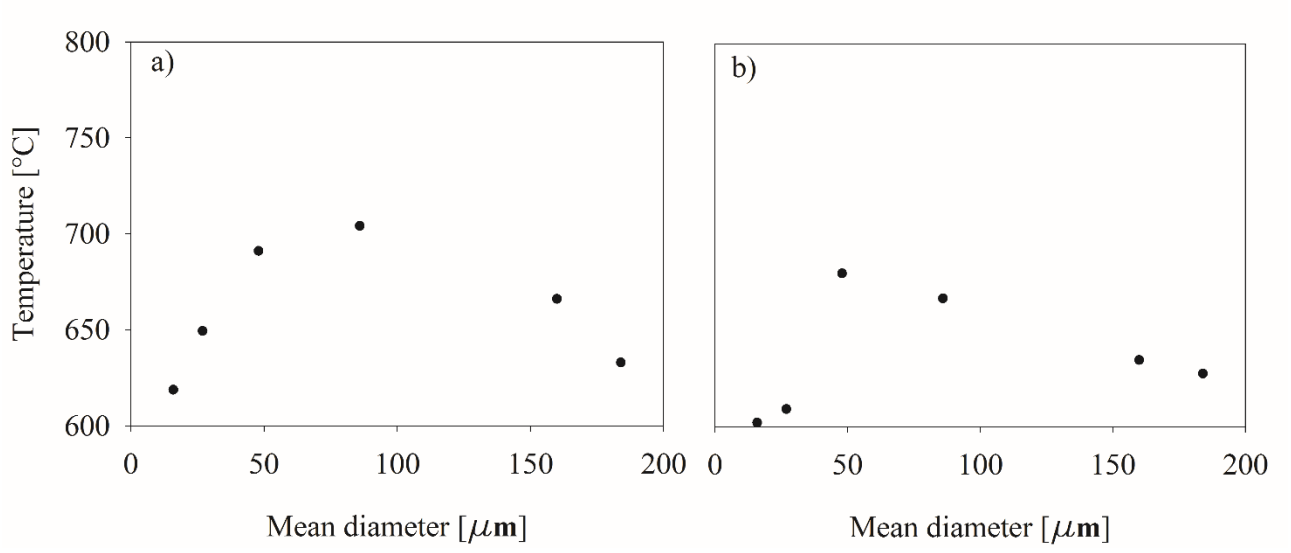

Figure 8. Sintering temperatures calculated solving Eqs (7) to (9) using the experimental neck diameter reported in table 2, a) low speed, b) high speed.

With the underlying hypothesis that only the energy necessary for sintering would be desired, we can estimate the efficiency of the laser energy use. Given the particle exposure times, t_{exp}, given in Eq (10), it is possible to define the heat balance on the heated spot. It turns out that the efficiency of the laser energy use for the purpose of sintering, η_l,would be .

$$\eta_l = \left[\frac{\pi d_{pi}^3}{6} \rho_p c_p \left(T_g - T_a\right) \left\{ \frac{\delta_l}{d_{pi}} \right\} \right] \Big/ \left(P_l \frac{d_{pi}^2}{d_{sp}^2} t_{exp} \right) \tag{11}$$

In Eq (11), P_l is the laser power, c_p is the specific heat of the particle material, T_g, is the sintering temperature, T_a the ambient temperature, δ_l the specimen thickness. In particular, the term in curly brackets in eq. (10) represents the average number of particles contained within the thickness of the sintered layer and accounts for the fact that the heating process does not involve a single particle layer only but the whole sintered layer thickness. The conditions tested are such that the product $P_l \cdot V_{sc}$ is constant and that t_{exp} is equal to 2.0 ms for the low scanning speed case and it is 1.0 ms for the high scanning speed case. Values of η_l, reported in Table 2, indicate a general low value of the efficiency of the laser energy use. Higher values are found for large particles for which only sintering is observed and therefore energy is not used for particle the melting, produced by heating the particles above the

nominal temperature value of T_g, appearing in Eq. (11). Another source of low efficiency values of the laser energy use is likely to be the heat dispersion in the material around the laser spotlight. Higher efficiencies at higher scanning speeds seem to suggest more limited heat dispersion for shorter exposure times, which may also explain the different sintering activation of the contact points between large and small particles at the different scanning speeds.

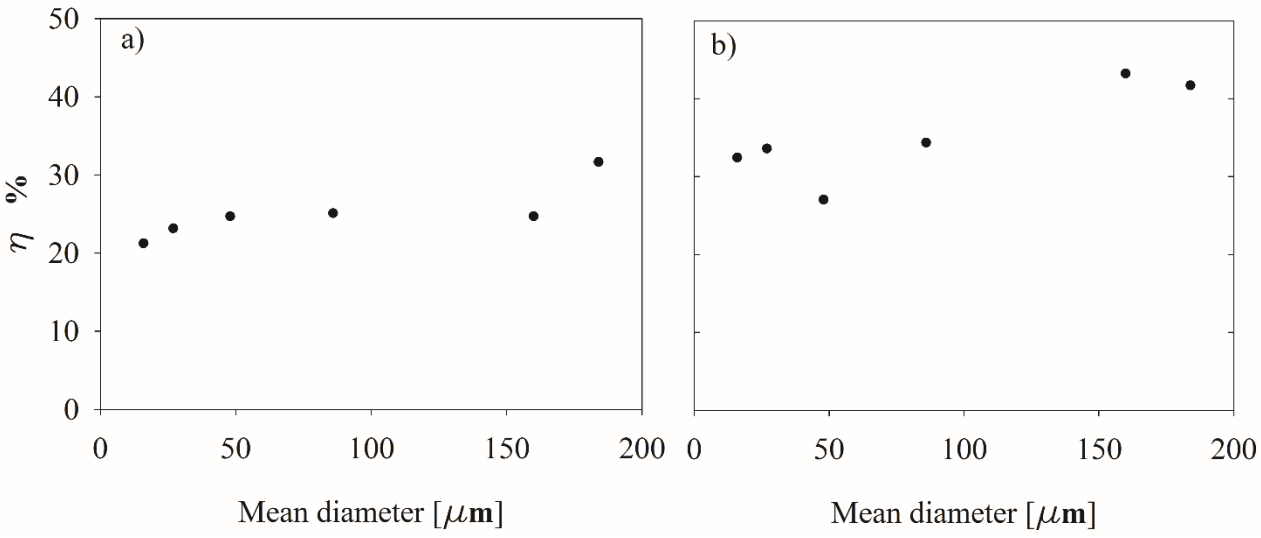

Figure 9. Efficiency of the laser energy calculated solving Eqs (11), a) low speed, b) high speed.

5. Conclusions

Microscopic observations on sintered materials and measures of mass, thickness and strength of single layer artifacts allow to characterize the effect of the main parameters in the laser sintering process.

The observation of the artifacts at the optical microscope allows to verify that the granular material directly subjected to irradiation of the laser has a high degree of fusion, while on the opposite side to that of the scan, the particles retain the original geometry. From experiments carried out on powder characterized by with narrow sized and unimodal particle size distribution it appears that an optimum in the sintered materials strength is obtained with particles sizes around 50 μm.

Table 2. Calculated sintered material properties according to eqs (4) to (6) at low scanning speed (laser power of 8W and scanning speed of 50 mm s^{-1}) and high scanning speed (laser power of 16W and scanning speed of 100 mm $s^{-1)}$.

Powder properties				**Low scanning speed**					**High scanning speed**				
d_{pi}	ρ_{bi}	ϕ_i	k	σ_i	F_{ci}	d_{ci}	η_l	T_g	σ_i	F_{ci}	d_{ci}	η_l	T_g
μm	kg m^{-3}	-	-	kPa	mN	μm	%	°C	kPa	mN	μm	%	°C
16	1370	0,547	6,85	1040	0,224	1,7	21	619	586	0,126	1,3	32	602
27	1410	0,562	7,07	1580	0,913	3,4	23	649	515	0,297	1,9	34	609
48	1480	0,58	7,39	2230	4,08	7,2	25	691	1880	3,17	6,4	27	680
86	1500	0,602	7,78	1970	9,77	11,2	25	704	855	4,24	7,4	34	666
160	1540	0,614	8,04	484	6,21	10	25	666	218	3,55	6,7	43	634
184	1540	0,616	8,07	182	3,89	7	32	633	155	3,32	6,5	42	628

The model by Rumpf and Molerus, generally used to correlate the bulk properties of the powders to the interparticle forces, has been employed for the interpretation of the results in terms of material strength. In particular, we have estimated the change of the neck size of particles by changing the particle size and the laser scanning speed. This data coupled with the Frenkel model allowed an estimate of the sintering temperature for the different experimental conditions tested. The common outcome is that the optimum strength corresponds also to the largest neck size and the highest sintering temperature. Furthermore the critical analysis of results analysis, seems also to suggest that the main difference occurring in the sintering process between low and high scanning speeds at equal released energy in the sintering process is the higher effectiveness of laser bean at high speed, most likely for the more limited effects of energy losses from the laser sintering spot.

Nomenclature

c_p specifc heat, W kg^{-1} K^{-1}

d_c, sintered contact diameter, m

398 d_p, particle diameter, m

399 d_s, mean sauter diameter, m

400 d_{sp}, size of the laser spot, m

401 f, fines fraction, -

402 F_c, interparticle force, N

403 k, particle coordination number, -

404 P_l laser power, W

405 T_a ambient temperature, K

406 t_{exp} particle exposure time, s

407 T_g glass transition temperature, K

408 t_{Hi} particle heating time, s

409 V_{sc} laser scanning speed, m s^{-1}

410 W_{LF} Effectiveness of contact between large an fine particles, -

411 *Greek*

412 δ_l, specimen thickness, m

413 ρ_b, powder bulk density, kg m^{-3}

414 ρ_P, particle density, kg m^{-3}

415 σ, tensile strength, N m^{-2}

416 σ_{tg}, glass tensile strength, N m^{-2}

417 ϕ, particle volume fraction, -

418 *Subscripts*

419 i, referred to a single unimodal narrow PSD sample

420 b, referred to a bimodal sample

421 F, referred to the fine fraction

L, referred to the coarse fraction

LF, referred to the large particles in contact with fines

References

[1] F.H. Liu, Synthesis of biomedical composite scaffolds by laser sintering: Mechanical properties and in vitro bioactivity evaluation, Appl. Surf. Sci. 297 (2014) 1–8. doi:10.1016/j.apsusc.2013.12.130.

[2] Y. Du, H. Liu, J. Shuang, J. Wang, J. Ma, S. Zhang, Microsphere-based selective laser sintering for building macroporous bone scaffolds with controlled microstructure and excellent biocompatibility, Colloids Surfaces B Biointerfaces. 135 (2015) 81–89. doi:10.1016/j.colsurfb.2015.06.074.

[3] L.S. Bertol, W.K. Júnior, F.P. da Silva, C. Aumund-Kopp, Medical design: Direct metal laser sintering of Ti-6Al-4V, Mater. Des. 31 (2010) 3982–3988. doi:10.1016/j.matdes.2010.02.050.

[4] W.E. Frazier, Metal Additive Manufacturing: A Review, J. Mater. Eng. Perform. 23 (2014) 1917–1928. doi:10.1007/s11665-014-0958-z.

[5] D.D. Gu, W. Meiners, K. Wissenbach, R. Poprawe, Laser additive manufacturing of metallic components: materials, processes and mechanisms, Int. Mater. Rev. 57 (2012) 133–164. doi:10.1179/1743280411Y.0000000014.

[6] S.K. Ghosh, P. Saha, Crack and wear behavior of SiC particulate reinforced aluminium based metal matrix composite fabricated by direct metal laser sintering process, Mater. Des. 32 (2011) 139–145. doi:10.1016/j.matdes.2010.06.020.

[7] G. Zhang, K. Feng, Y. Li, H. Yue, Effects of sintering process on preparing iron-based friction material directly from vanadium-bearing titanomagnetite concentrates, Mater. Des. 86 (2015) 616–620. doi:10.1016/j.matdes.2015.07.162.

[8] E. Salahinejad, R. Amini, M. Marasi, M.J. Hadianfard, The effect of sintering time on the densification and mechanical properties of a mechanically alloyed Cr-Mn-N stainless steel, Mater. Des. 31 (2010) 527–532. doi:10.1016/j.matdes.2009.07.024.

[9] B. Yao, H. Su, J. Zhang, Q. Ren, W. Ma, L. Liu, H. Fu, Sintering densification and microstructure formation of bulk Al2O3/YAG eutectic ceramics by hot pressing based on fine eutectic structure, Mater. Des. 92 (2016) 213–222. doi:10.1016/j.matdes.2015.12.017.

[10] P. Regenfuss, a Streek, L. Hartwig, Advancements in laser micro sintering, Proc. Third Int. WLT-Conference Lasers Manuf. 2005, Munich, June 2005. (2005) 2–5.

[11] E.O. Olakanmi, R.F. Cochrane, K.W. Dalgarno, A review on selective laser sintering/melting (SLS/SLM) of aluminium alloy powders: Processing, microstructure, and properties, Prog. Mater. Sci. 74 (2015) 401–477. doi:10.1016/j.pmatsci.2015.03.002.

[12] F.E. Wiria, K.F. Leong, C.K. Chua, Modeling of powder particle heat transfer process in selective laser sintering for fabricating tissue engineering scaffolds, Rapid Prototyp. J. 16 (2010) 400–410. doi:10.1108/13552541011083317.

[13] a. Streek, P. Regenfuss, H. Exner, Fundamentals of Energy Conversion and Dissipation in Powder Layers during Laser Micro Sintering, Phys. Procedia. 41 (2013) 858–869. doi:10.1016/j.phpro.2013.03.159.

[14] F. Calignano, D. Manfredi, E.P. Ambrosio, S. Biamino, M. Pavese, P. Fino, Direct Fabrication

of Joints based on Direct Metal Laser Sintering in Aluminum and Titanium Alloys, Procedia CIRP. 21 (2014) 129–132. doi:10.1016/j.procir.2014.03.155.

[15] D. Gu, Y. Shen, Balling phenomena in direct laser sintering of stainless steel powder: Metallurgical mechanisms and control methods, Mater. Des. 30 (2009) 2903–2910. doi:10.1016/j.matdes.2009.01.013.

[16] S.S. Deng, D.J. Wang, Q. Luo, Y.J. Huang, J. Shen, Spark plasma sintering of gas atomized AlNiYLaCo amorphous powders, Adv. Powder Technol. 26 (2015) 1696–1701. doi:10.1016/j.apt.2015.10.009.

[17] Y. Wang, D. Rouholamin, R. Davies, O.R. Ghita, Powder characteristics, microstructure and properties of graphite platelet reinforced Poly Ether Ether Ketone composites in High Temperature Laser Sintering (HT-LS), Mater. Des. 88 (2015) 1310–1320. doi:10.1016/j.matdes.2015.09.094.

[18] B. Qian, Z. Shen, Journal of Asian Ceramic Societies Laser sintering of ceramics, Integr. Med. Res. 1 (2013) 315–321. doi:10.1016/j.jascer.2013.08.004.

[19] A. Cerardi, M. Caneri, R. Meneghello, G. Concheri, M. Ricotta, Mechanical characterization of polyamide cellular structures fabricated using selective laser sintering technologies, Mater. Des. 46 (2013) 910–915. doi:10.1016/j.matdes.2012.11.042.

[20] A. Verma, S. Tyagi, K. Yang, Modeling and optimization of direct metal laser sintering process, Int. J. Adv. Manuf. Technol. 77 (2015) 847–860. doi:10.1007/s00170-014-6443-x.

[21] X. Tian, J. Günster, J. Melcher, D. Li, J.G. Heinrich, Process parameters analysis of direct laser sintering and post treatment of porcelain components using Taguchi's method, J. Eur. Ceram. Soc. 29 (2009) 1903–1915. doi:10.1016/j.jeurceramsoc.2008.12.002.

[22] P. Bertrand, F. Bayle, C. Combe, P. Goeuriot, I. Smurov, Ceramic components manufacturing by selective laser sintering, Appl. Surf. Sci. 254 (2007) 989–992. doi:10.1016/j.apsusc.2007.08.085.

[23] Y. Tang, Direct laser sintering of a silica sand, Mater. Des. 24 (2003) 671–679. doi:10.1016/S0261-3069Ž03.00126-2.

[24] M.A. Hussein, C. Suryanarayana, M.K. Arumugam, N. Al-Aqeeli, Effect of sintering parameters on microstructure, mechanical properties and electrochemical behavior of Nb-Zr alloy for biomedical applications, Mater. Des. 83 (2015) 344–351. doi:10.1016/j.matdes.2015.06.003.

[25] R.C. J. Seville, U. Tüzün, Processing of Particulate Solids, 1997. doi:10.1007/978-94-009-1459-9.

[26] C. Luan, C. You, A novel experimental investigation into sintered neck tensile strength of ash at high temperatures, Powder Technol. 269 (2015) 379–384. doi:10.1016/j.powtec.2014.09.031.

[27] D. Sofia, M. Granese, D. Barletta, M. Poletto, "Laser Sintering of Unimodal Distributed Glass Powders of Different Size," Procedia Eng. 102 (2015) 749–758. doi:10.1016/j.proeng.2015.01.180.

[28] S. Berretta, O. Ghita, K.E. Evans, A. Anderson, C. Newman, Size, shape and flow of powders for use in Selective Laser Sintering (SLS), 6th Int. Conf. Adv. Res. Virtual Phys. Prototyping, VR@P 2013, Oct. 1, 2013 -. (n.d.) 49–54.

[29] J. Ibbett, B. Tafazzolimoghaddam, H. Hernandez Delgadillo, J.L. Curiel-Sosa, What triggers a microcrack in printed engineering parts produced by selective laser sintering on the first place?, Mater. Des. 88 (2015) 588–597. doi:10.1016/j.matdes.2015.09.026.

[30] K. Senthilkumaran, P.M. Pandey, P.V.M. Rao, Influence of building strategies on the accuracy of parts in selective laser sintering, Mater. Des. 30 (2009) 2946–2954. doi:10.1016/j.matdes.2009.01.009.

[31] N.K. Tolochko, K.I. Arshinov, S.Z. Mozzharov, Selective laser sintering of compacted powders, Powder Metall. 37 (1998) 365–368. http://www.springerlink.com/index/H567032241266227.pdf.

[32] H. Rumpf, Grundlagen und Methoden des Granulierens, Chemie Ing. Tech. - CIT. 30 (1958) 144–158. doi:10.1002/cite.330300307.

[33] O. Molerus, Theory of yield of cohesive powders, Powder Technol. 12 (1975) 259–275. doi:10.1016/0032-5910(75)85025-X.

[34] P.F. Smith, W. O., Foote, P. D., Busang, Packing of homogeneous spheres, Phys. Rev. 34 (1929) 1271–1274.

[35] M.M. Ristić, S.D. Milosević, Frenkel's Theory of Sintering, Sci. Sinter. 38 (2006) 7–11. doi:10.2298/SOS0601007R.

[36] G. Guan, M. Hirsch, Z.H. Lu, D.T.D. Childs, S.J. Matcher, R. Goodridge, K.M. Groom, A.T. Clare, Evaluation of selective laser sintering processes by optical coherence tomography, Mater. Des. 88 (2015) 837–846. doi:10.1016/j.matdes.2015.09.084.

[37] F.T. Wallenberger, P.A. Bingham, Fiberglass and glass technology: Energy-friendly compositions and applications, 2010. doi:10.1007/978-1-4419-0736-3.

[38] K.C. Lyon, Calculation of surface tensions of glasses, J. Am. Ceram. Soc. 27 (1942) 25–28. doi:10.1111/j.1151-2916.1944.tb14889.x.